Computation & theory

Growth modes of grain boundary precipitate in aluminum alloys under different lattice misfits

X. Shuai[1], H. Mao[1], S. Tang[2],[*] (iD), Y. Kong[1], and Y. Du[1],[*]

[1] *State Key Lab for Powder Metallurgy, Central South University, Changsha 410083, Hunan, China*
[2] *National Key Laboratory of Science and Technology On High-Strength Structural Materials, Central South University, Changsha 410083, China*

ABSTRACT

The properties of aluminum alloys are profoundly affected by a rich variety of precipitates. Their precipitation behaviors are often very different from each other due to a wide range of lattice misfits between the precipitates and the matrix. This makes the study of mechanisms of the formation of aluminum alloy precipitates very complex and often controversial. Here, the phase-field crystal methodology is used to study grain boundary (GB) precipitation under different lattice misfits. We find that the growth mode of GB precipitation changes from island growth mode to layer growth mode with increasing lattice misfit. At a relatively low lattice misfit, GB segregation and spinodal decomposition first lead to the heterogeneous distribution of solute and then nucleation events at solute-enriched sites, which is conducive to the island growth of the nuclei. In contrast, at a sufficiently high lattice misfit, a layer with a high solute concentration is formed soon along the entire GB due to a great amount of solute segregation, which gives rise to the rapid merging of densely distributed nuclei, and then layer growth occurs. Quantitative analysis reveals that the increase in lattice misfit decreases the nucleation barrier and the critical concentration required by the onset of structural transformation. Our study contributes to a systematic understanding of the formation of diversified precipitates in aluminum alloys in terms of lattice misfit.

GRAPHICAL ABSTRACT
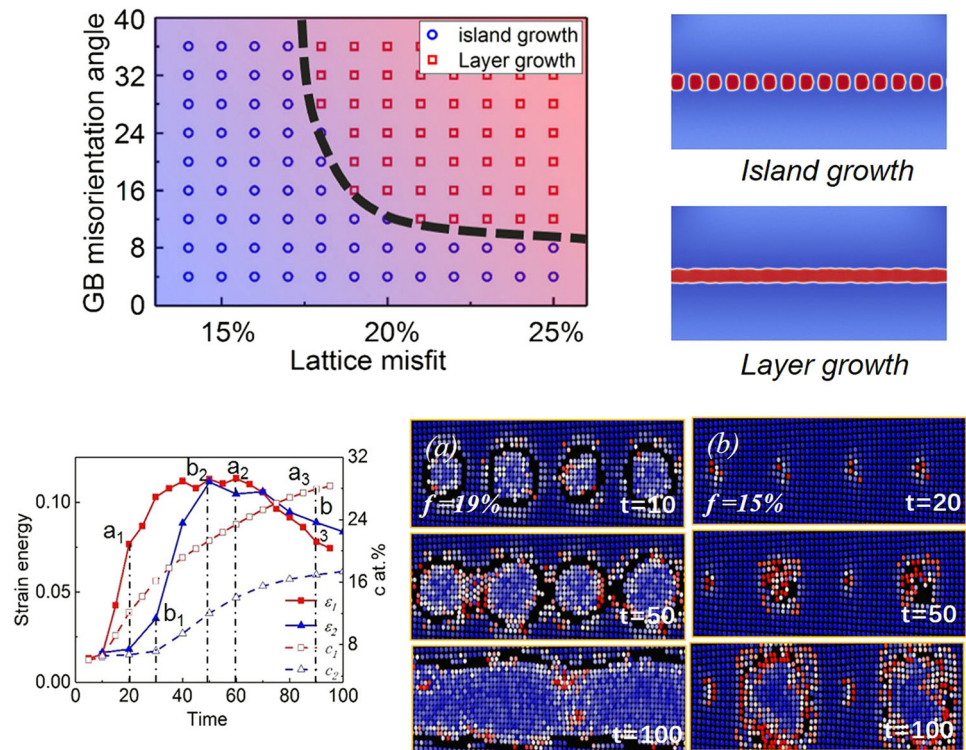
Introduction

Elastic strain exists widely in polycrystalline materials, especially in grain boundaries (GBs) [1–4]. It plays a crucial role in the solid–solid phase transformations of alloys [5–10]. Lattice misfit can induce coherent elastic strain between the matrix and precipitated phases [5, 8] and thus exert substantial influences on the microstructure of precipitates. This is particularly significant for precipitation-strengthening alloys such as aluminum alloys, which are characterized by a rich variety of precipitates. The coherency of the precipitate-matrix interface, number density, size, and precipitation behaviors of such precipitates may be very different from each other and depend profoundly on the magnitude of the lattice misfit [11–16]. It has been estimated that the lattice misfits at the precipitate-matrix interface range from approximately 1% to over 20% [11, 12, 16]. Such a wide range of lattice misfits leads to very different

pictures of precipitation in aluminum alloys. Previous studies have elucidated the kinetics and mechanisms about precipitation of some precipitates, e.g., the precipitation sequence of the Al_2Cu phase. However, we lack a comprehensive understanding of the formation of such diversified precipitates. The key is to acquire the dependence of precipitation behaviors on the magnitude of lattice misfit.

Lattice misfit has considerable impacts on the misfit strain and coherence of interfaces, which profoundly influences the growth mode of GB precipitation [17, 18]. Kim et al. [19, 20] reported that a microstructure with a low-level lattice misfit shows a typical core/rim structure with faceted grains in Ti(C0.7N0.3)–WC–Ni systems. However, increasing the lattice misfit results in the formation of solid solution grains without Ti(C, N) cores. Wen H. et al. also observed the layer and island growth modes in the case of $M_{23}C_6$ precipitates in GBs and regarded that such an apparent discrepancy could be partly attributed to the variation of the magnitude of lattice

misfits between precipitates and the matrix grains [21]. Experimental and modeling studies have revealed that the coarsening behaviors of GB precipitates are also influenced by lattice misfit [22–24]. The coarsening constant of multicomponent L_{12} particles decreases with the increasing lattice misfit in high entropy alloys [25]. These previous studies have demonstrated the profound influences of lattice misfits on precipitation. Nevertheless, the quantification of such influences is still challenging because it is often difficult to change the magnitude of lattice misfits over a wide range in real alloys. As a result, the microscopic mechanisms related to such influences are still unclear. These problems prevent us from a deep understanding of precipitation processes affected by lattice misfit. Clarifying the dependences of precipitation behaviors on lattice misfit can help us to obtain a systematic understanding of the mechanisms for the nucleation and growth of precipitates in aluminum alloys.

Recently, many studies have demonstrated that low-dimensional spinodal decomposition along the GB plays a crucial role in GB precipitation [26–29]. It was reported that GB segregation and spinodal decomposition are strongly affected by the local strain in the GB [30–32]. The lattice misfit greatly changes the local strains in the GB and brings about more unexpected effects on compositional evolution along the GB [33, 34]. A systematic study of the interactions among structural, compositional, and coherent strain evolutions during GB precipitation is the key to revealing the microscopic mechanisms related to the effect of lattice misfits. Atomic-scale studies of GB precipitation can provide the most direct picture of such evolution.

There are formidable challenges for the experimental characterization of GB precipitation in real-time on the atomic scale [35, 36]. Continuum numerical simulation methodologies such as the phase-field method are unable to reveal atomic scale information of compositional and structural evolution [37]. Molecular dynamics (MD) [38, 39] and Monte Carlo (MC) [40, 41] simulations have been used to study phase transitions in GBs, but none of these methods can reveal the dynamic evolution on the diffusion time scale. The phase-field crystal (PFC) model [42–46] can describe material processes over diffusion time scales with resolutions up to the atomic scale. Over the last decades, this methodology has been utilized to successfully study crystal

nucleation [46, 47], grain growth [44, 48–51], precipitation [52–54], crystal defect dynamics [55–57], and so on.

In this work, the PFC model was employed to study GB precipitation of the precipitates in aluminum alloys with magnitudes of lattice misfits spanning a wide range. The changes in GB precipitation behavior with lattice misfit are focused. Firstly, we investigate the processes of GB precipitation under various lattice misfits. A schematic map of the selection of the growth mode of precipitates with respect to lattice misfit and GB structure is summarized accordingly. Then, we analyze the evolution of the atomic configuration structure, composition, and misfit strain energy during the early stage of precipitation. These results contribute to a deep understanding of the influences of lattice misfit on GB precipitation by revealing microscopic views for such evolution processes.

Method

Structural phase-field crystal model (XPFC model)

The free energy functional in the binary PFC model is written as follows [58]:

$$
\begin{aligned}
\frac{\Delta F}{kT\rho^o} &= \int f \mathrm{d}r \\
&= \int \left\{ \begin{array}{l} \dfrac{n^2}{2} - \eta\dfrac{n^3}{6} + \chi\dfrac{n^4}{12} + (n+1)\Delta F_{\mathrm{mix}} \\ -\dfrac{1}{2}n\int \mathrm{d}r' C_{\mathrm{eff}}^n(|r-r'|)n' + \alpha|\vec{\nabla}c|^2 \end{array} \right\} \mathrm{d}r,
\end{aligned}
$$

$$(1)$$

where n represents the reduced dimensionless atomic number density and c the solute concentration fields. η and χ are introduced to fit the ideal energy to a polynomial expansion. α is related to the energy of compositional interfaces (assume $\alpha = 1$). The entropy of mixing

$$
\Delta F_{\mathrm{mix}} = \omega\left\{ c\ln\left(\frac{c}{c_o}\right) + (1-c)\ln\left(\frac{1-c}{1-c_o}\right) \right\},,
\qquad (2)
$$

where the coefficient ω is used to fit the entropic energy away from the reference composition c_0. These parameters are discussed further in Ref [44]. For a binary alloy, Greenwood et al. [45] defined the effective correlation function,

Table 1 Parameters of PFC simulations

parameters	Symbols	Values/Expressions
Reference density	ρ^0	0.01
Reference composition	c_0	0.5
Polynomial fitting parameters	η, χ	$\eta = 1.4$, $\chi = 1$
Entropy of mixing coefficient	ω	0.005
Parameters for correlation function	σ_{Mi}, α_i	$\sigma_{Mi} = 0.6$, $\alpha_i = 0.8$
Gradient energy coefficient	α	1

$$C_{\text{eff}}^n = X_1(c)C_2^{\text{AA}} + X_2(c)C_2^{\text{BB}} \qquad (3)$$

where

$$X_1(c) = 1 - 3c^2 + 2c^3$$
$$X_2(c) = 1 - 3(1-c)^2 + 2(1-c)^3, \qquad (4)$$

C_2^{AA} and C_2^{BB} are correlation functions for pure elements A and B, respectively. The correlation functions $\widehat{C}_2^{ii}(i = A\,or\,B)$ are defined to include reciprocal space peaks at positions determined by each component's equilibrium crystal unit cell structure. Each peak is represented by the following Gaussian form reading:

$$\hat{C}_{2j}^{ii} = e^{-\frac{\sigma^2}{\sigma_{Mj}^2}} e^{-\frac{(k-k_j)^2}{2\sigma_j^2}}, \qquad (5)$$

where ii = AA, BB, σ_{Mj} is the sufficient transition temperature and α_j is the width of the Gaussian peak, which is modulated for temperature by a Debye–Waller prefactor. The total kernel $\widehat{C}_{2j}^{ii}$ is taken as the envelope of all peaks $\widehat{C}_{2j}^{ii}$ included to represent the atomic interactions. The total density is defined as the accumulation of the density of each component ($\rho = \rho_A + \rho_B, \rho^o = \rho_A^o + \rho_B^o$). The equations of motion are written as

$$\frac{\partial n}{\partial t} = \vec{\nabla} \cdot \left\{ M_n \vec{\nabla} \left(\frac{\delta F}{\delta n} \right) \right\} \qquad (6)$$

$$\frac{\partial c}{\partial t} = \vec{\nabla} \cdot \left\{ M_c \vec{\nabla} \left(\frac{\delta F}{\delta c} \right) \right\} \qquad (7)$$

where $n = \rho/\rho^o - 1$ and $c = \rho_B/\rho$. M_n and M_c are dimensionless kinetic mobility parameters (assumed to be equal to 1).

Simulation details

Four samples containing two-grain boundaries were prepared on a 2-D rectangular mesh with a grid spacing dx = 0.125 and a time step dt = 0.05. The size of the simulation box was 3840*3840 grid spacing (equivalent to 480*480 atoms). Each atomic spacing was resolved by eight mesh spacings considering a lattice parameter of 1 for a 2-D square structure. To solve the dynamic equations, a semi-implicit algorithm was used in Fourier space for high efficiency [59]. The initial condition is two grains separated by a tilt symmetric GB. Two steps are needed to generate this initial condition. First, we place two abutting crystals, which are separated by a liquid film with a width of approximately 10 grid points. The purpose of the introduction of the liquid film is to give rise to a relaxed GB. Once the simulation starts, the liquid film disappears soon and is replaced by the GB we need. Second, we reset the initial value within the composition of the whole simulation box and restart the simulation of GB precipitation. The GB misorientation angles of the low-angle GB and the high-angle GB are 4° and 36.5°, respectively. Both GBs are along the Y direction, with one located at $x = L/4$ and the other at $x = 3L/4$. The initial concentration is a uniform field with a solute concentration of c_0. Other parameters for PFC simulations are listed in Table 1.

Results and discussion

In this section, we discuss the growth modes of GB clusters as a function of lattice misfit and GB misorientation. The lattice misfit f is defined as $f = (a_0 - a_1)/a_0$, where a_0 and a_1 are the lattice constants of the matrix and precipitates, respectively. The magnitudes of lattice misfits range from 14 to 25%. This is based on aluminum alloys with plenty of precipitates. The lattice misfits between the matrix and precipitates in Al-based alloys range from very small (Al₃Zr, 0.27%) to very large (δ-AlLi, 21.4%) [11, 12, 60]. Our simulations are not limited to the formation of a specific precipitate of aluminum

alloys. However, in the pursuit of the generality of generality in this study, plenty of precipitates of aluminum alloys are included in our simulation in the clue of lattice misfit.

The growth modes and kinetics of GB precipitation under different lattice misfits

Figure 1 presents the nucleation and growth of GB precipitates under different magnitudes of lattice misfit at low and high angles tilt GB. At the nucleation stage, the number of nuclei increases with lattice misfits, and the nuclei distribute discretely even in the case of relatively high lattice misfits. In contrast, at the growth stage, two distinct modes—island growth and layer growth—are observed. Island growth has been widely observed in many alloy systems [61], while layered growth has only been observed in some special maraging alloys [62] and superalloys [63, 64]. Our PFC simulations reveal in detail the scenario of the two growth modes. The island growth mode in Fig. 1b and d corresponding to a relatively low lattice misfit ($f = 15\%$) is characterized by a bunch of individual precipitates. Neighboring precipitates are separated by the matrix phase. The extension of a cluster along the GB is hindered because the growth of clusters normal to the GB has priority in the competition for feeding solutes diffused from the bulk of abutting gains. The layer growth mode in Fig. 1a and b first undergo the rapid coalesce of neighboring clusters due to sufficiently segregated solute and then the prevalence of the layer growth mode. Layer growth becomes increasingly prevalent as lattice misfit increases. There are two reasons to explain this. First, by comparing Fig. 1a with b or c with d, we can see that a sufficiently high lattice misfit ($f = 19\%$) can promote

the nucleation of GB clusters (this will be explained later). Thus, neighboring clusters merge soon due to very small distances between them. Second, the increase of lattice misfit makes lattice distortion more severe and promotes solute enrichment at GBs.

However, the degree of lattice misfit is not the sole factor. The GB structure also affects the growth mode of GB clusters. We summarize in Fig. 2 the selection map of the growth mode with respect to lattice misfit and GB misorientation. It is demonstrated that the layer growth mode becomes more popular with the increasing misorientation of GBs at a fixed lattice misfit. A sufficient and homogeneous solute film tends to form at high angle tilt GBs, which is conducive to the layer growth mode.

Although the nucleation mechanism at the onset of the two growth modes does not vary with lattice misfit, the nucleation kinetics depend closely on it. As shown in Fig. 1, the number density of nuclei increases with the magnitude of lattice misfit. Additionally, the incubation time decreases exponentially (Fig. 3a), suggesting the strong influences of lattice misfit on the nucleation of GB precipitates. These influences are attributed to the total work of formation.
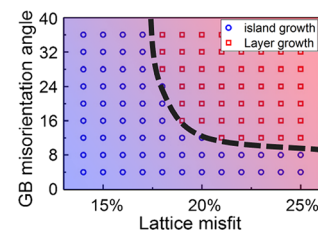
Figure 2 The sketch about the selection of growth modes of GB clusters with respect to GB misorientation angle and lattice misfit.

Figure 1 GB precipitation processes with different lattice misfits. **a** Low-angle tilt GB with lattice misfit 19%; **b** Low-angle tilt GB with lattice misfit 15%; **c** High-angle tilt GB with lattice misfit 19%; **d** High-angle tilt GB with lattice misfit 15%.
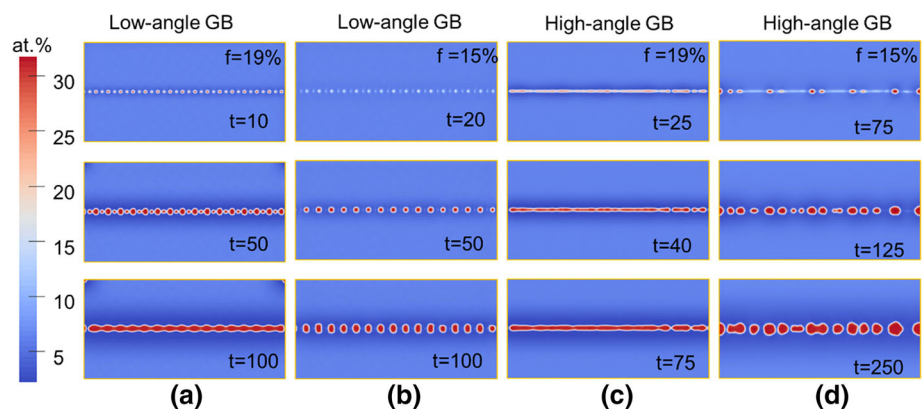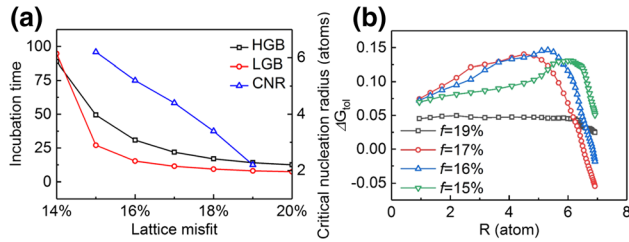
Figure 3 The kinetics analysis of GB precipitation. **a** The nucleation incubation time vs. lattice misfit for a high angle tilt GB (HGB) and a low angle tilt GB (LGB), and the curve with triangle symbol shows the change of critical nucleation radius (CNR) with lattice misfit. **b** The total formation work.

The total work of formation was calculated based on the variation of the energy of the local area around the nucleation site during GB precipitation [53, 54]. We calculated the change in the grand potential within some small boxes, including nucleated clusters in these samples. A total of 32 nucleated clusters are considered in the calculation. ΔG_{tol} is expressed as follows:

$$
\begin{aligned}
\Delta G_{tot} &= \int_V \omega - \int_V \omega^b \\
&= \int_V [f - \mu_c \cdot c - \mu_n \cdot n] \\
&\quad - \int_V [f^b - \mu_c^b \cdot c^b - \mu_n^b \cdot n^b].
\end{aligned}
\tag{8}
$$

where f is the free energy functional calculated by Eq. 2, $\mu_c = \delta f/\delta c$ and $\mu_n = \delta f/\delta n$ are the diffusion potentials of the concentration and density fields, respectively, and V is the total volume [54]. c is the concentration, and the subscribe b represents the bulk phase. The total work of formation, as shown in Fig. 3b, is calculated at various misfits and GB structures. The abscissa corresponding to the peak of the total work of formation represents the critical nucleation radius. The critical nucleation radius decreases as lattice misfit increases. Thus, an increase in lattice misfit favors cluster nucleation. Next, we will discuss the underlying mechanisms of the two growth modes related to structural evolution, solute transportation, and the evolution of coherent strain.

The atomic-scale mechanism of structural evolution

The low-angle tilt GB in Fig. 4 is constituted by an array of dislocation pairs. Sites A and B correspond to

paring dislocations. As quantified in Fig. 4a and d, the concentration of site B is much higher than that of site A before the nucleation of clusters. Normally, as shown in Fig. 4d–f, nucleation usually does not occur at site A because of insufficient concentration. Nevertheless, the scenario may change as lattice misfit increases. Figures 4a–c shows that clusters form at both sites A and B with a higher lattice misfit of 19%. At site A of Fig. 4a, we observe that the structural evolution in these dislocations first undergoes a short stage of a disordered state and then the formation of a precipitated phase (Fig. 4b). However, no disordered structure appears at site B in the case of both lattice misfits. The evolution of the compositional profiles suggests that lattice misfit strongly influences the mass transportation along the GB, which promotes nucleation at sites (sites A, for example) having no priority in the case of relatively low lattice misfit (15%). Interestingly, two distinct growth modes corresponding to the two cases of lattice misfits are observed after nucleation. The neighboring clusters coalesce into a layer in the case of the relatively high lattice misfit (19%), while the clusters in the case of the lower lattice misfit (15%) tend to grow into the abutting grains, resulting in island-shaped precipitates.

Figure 5 shows the nucleation of clusters at high-angle tilt GBs. At the early stage of nucleation, the solute shows uniform enrichment along the GB and forms a continuous precipitation layer on the high-angle tilt GB when the lattice misfit is 19%. The initial clusters, also called embryos, show structural disorder. Then, the disorder precursors transform into a stable square phase structure. The cluster nucleation at the high-angle tilt GB with a lower lattice misfit of 15% is a different picture. The solute enrichment controlled by segregation and spinodal decomposition contributes to the formation of small disconnected clusters, as shown in Fig. 5d. First, the matrix is decomposed into disordered structures. Then, two nuclei are nucleated at the matrix-disordered structure interfaces, and a new GB is formed when the two nuclei meet, as shown in Fig. 5e. Experimental evidence for such two-layer GB precipitates has been found in several alloy systems [21, 62]. We conjecture that a perfect symmetric tilt GB may be conducive to the formation of such double precipitates.

To confirm the lattice structure during the GB phase transformation, we calculated the radial distribution function (RDF) around nucleation sites. The

Figure 4 The structural and compositional evolution of GB precipitation in the low-angle tilt GB. Relatively high lattice misfit: **a** t = 10; **b** t = 50; **c** t = 100. Relatively low lattice misfit: **d** t = 20; **e** t = 50; **f** t = 100. The yellow curves represent the concentration of solute around the GB.
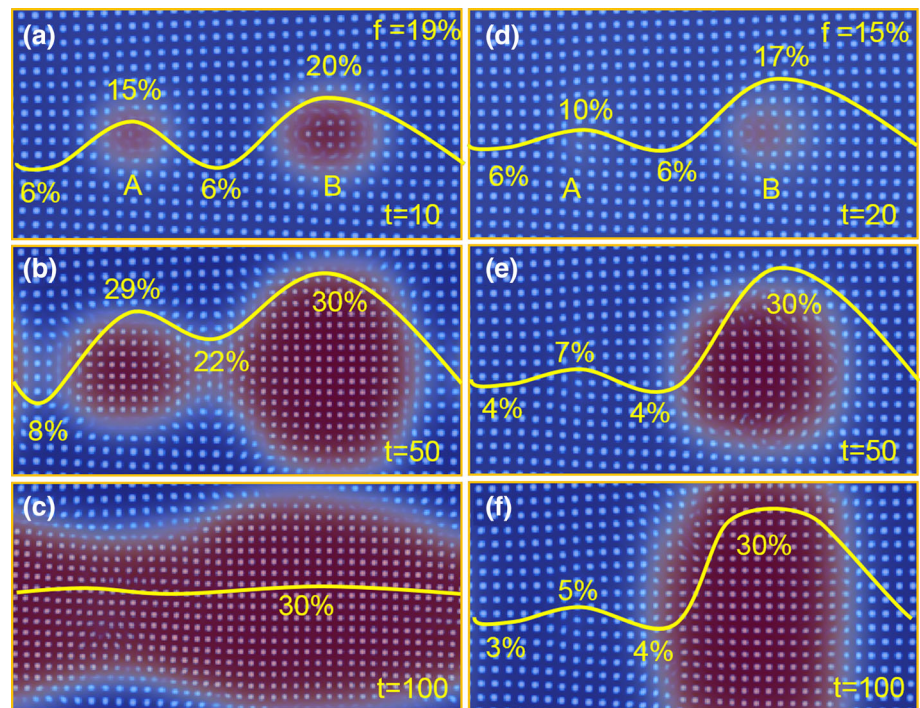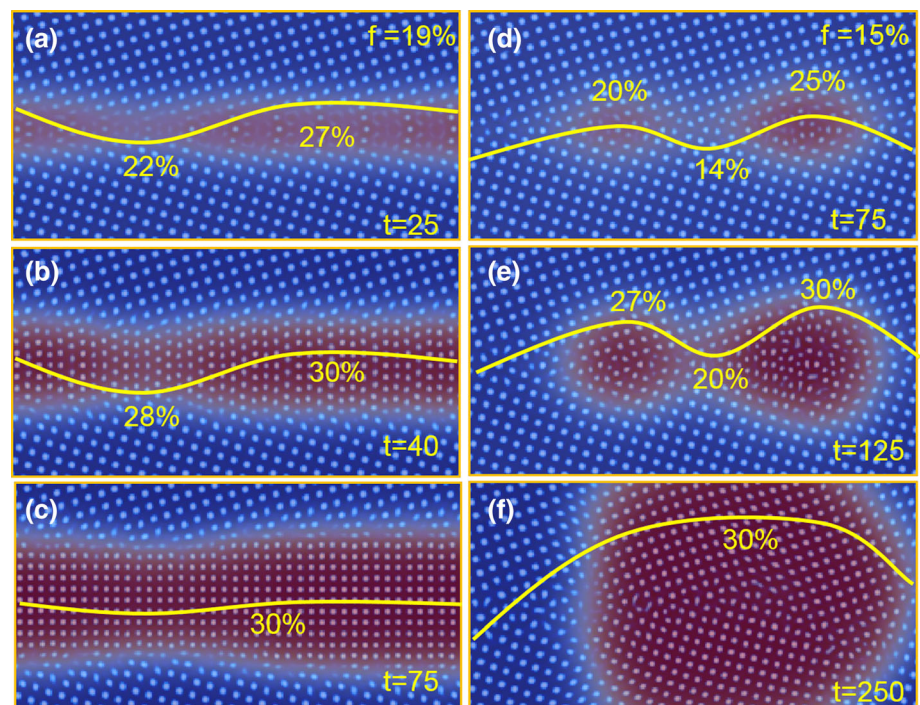

Figure 5 The structural and compositional evolution of GB precipitation in the high-angle tilt GB. Relatively high lattice misfit: **a** t = 10; **b** t = 50; **c** t = 100. Relatively low lattice misfit: **d** t = 20; **e** t = 50; **f** t = 100. The yellow curves represent the concentration of solute around the GB.

RDFs of a low-angle tilt GB with lattice misfits of 19% (Fig. 6a) and 15% (Fig. 6b) have sharp peaks, which indicates that the lattice structure maintains a certain degree of order during the process of precipitation. This can be verified by the atomic configurations of the structural transformation in Fig. 4. The red curves in Fig. 6c and d present a relatively gentle secondary peak, suggesting a disordered structure. The green curves indicate that the lattice structures evolve into a new square structure with a different lattice constant.
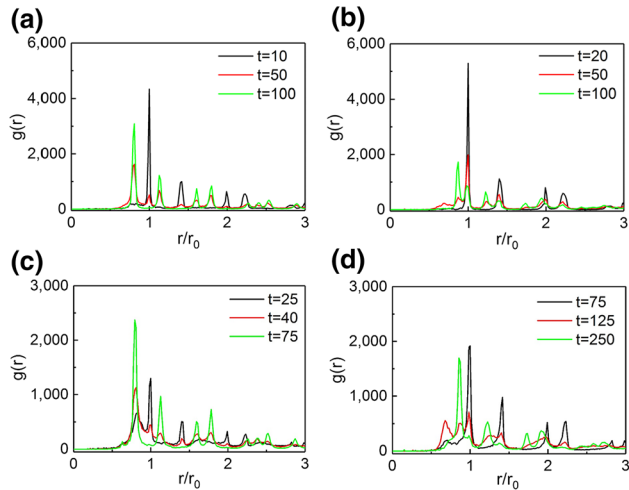
Figure 6 Time evolution of radial distribution functions of GB clusters. **a** Low-angle tilt GB with lattice misfit 19%; **b** Low-angle tilt GB with lattice misfit 15%; **c** high-angle tilt GB with lattice misfit 19%; **d** High-angle tilt GB with lattice misfit 15%.

Compositional evolution

Atomic-scale structural evolution cannot be realized without mass transportation. We quantify the solute transportation for the two growth modes observed above. Figure 7 describes the concentration evolution around nucleation sites at the low-angle tilt GB and the high-angle tilt GB. The evolution of concentration can be divided into two stages according to the increase in concentration with time. During stage I, the concentration increases linearly to a critical concentration (approximately 10% for the low-angle tilt GB and 14% for the high-angle tilt GB). The influence of the lattice misfit on the concentration enrichment rate at this stage is not distinct. We speculate that the concentration evolution in this stage is mainly attributed to solute segregation from the abutting grains to the GBs. In stage II, the concentration increases nonlinearly, and the concentration
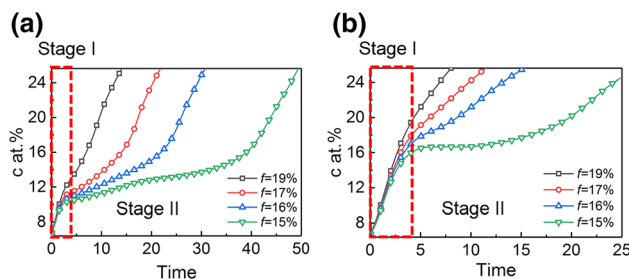
enrichment rate increases with the magnitude of lattice misfit. The compositional evolution in this stage is mainly controlled by the low-dimensional spinodal decomposition along the GBs [52, 65], which results in a rapid increase in solute concentration at nucleation sites.

The evolution of solute concentration demonstrates that the competition between island growth and layer growth mode is determined by the amount of solute segregated from the bulk of grains. The increase in lattice misfit greatly promotes such mass transportation. Figure 8 presents the concentration profiles along the low-angle and high-angle tilt GBs obtained under different lattice misfits. At the initial stage of compositional evolution, all the solute concentration profiles oscillate periodically. Subsequently, in the case of the higher lattice misfit (Fig. 8a, c), the amplitude of the concentration profiles decreases because of the rapid increase in the concentration at the valleys (regions between nuclei). Finally, a uniform concentration is attained, corresponding to the layer growth mode. However, in the case of the lower lattice misfit (Fig. 8b, d), the peaks and valleys of concentration profiles are alternately distributed along GBs, and the amplitudes of the oscillating concentration profiles increase with time. The low concentration regions (valleys) inhibit the merging of neighboring nuclei, which contributes to the island growth mode. It is demonstrated that a higher lattice
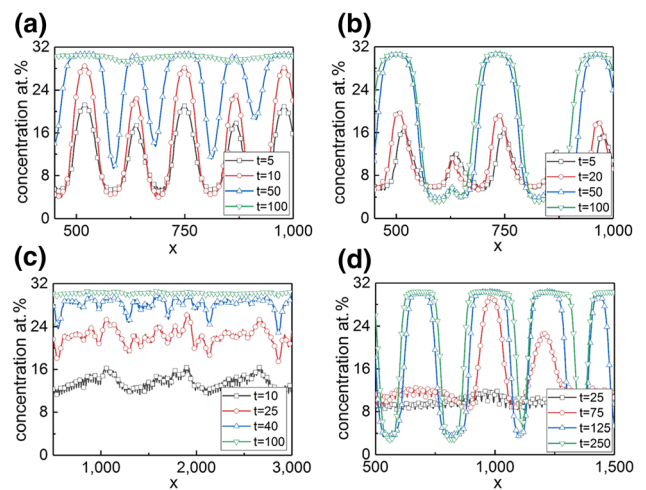

Figure 8 The time evolution of composition field along GB. **a** Low-angle tilt GB with lattice misfit 19%; **b** Low-angle tilt GB with lattice misfit 15%; **c** high-angle tilt GB with lattice misfit 19%; **d** High-angle tilt GB with lattice misfit 15%.

Figure 7 The averaged concentration evolution around the entire GB. **a** Low-angle tilt GB; **b** High-angle tilt GB.

misfit tends to cause GBs to absorb more solutes and form a more homogeneous concentration layer.

The evolution of coherent strain

The lattice misfit can directly influence the misfit strain distribution of GBs before precipitation and the coherent strain of the interface between the matrix and precipitates after precipitation. We calculate the strain energy distribution around GB clusters during the whole nucleation process by the peak pair algorithm [66, 67]. As shown in Fig. 9a–d, the enriched solute atoms greatly distort the lattice structure at the GBs, making the misfit strain in the GB region increase profoundly. In return, the increase in misfit strains promotes GB solute enrichment, contributing to a positive feedback effect. There are many vacancies at the interface between the precipitate phase and the matrix phase in the case of high lattice misfit. As a classical model of precipitation, the precipitation sequence in Al-Cu alloys Al SS → G.Pzone → θ''-

Al$_3$Cu → θ' -Al$_2$Cu → θ-Al$_2$Cu also involves different magnitudes of lattice misfits between precipitates and matrix. θ''-Al$_3$Cu (L12 lattice, a = 0.405 nm, c = 0.770 nm) [12] with a misfit of 0.25% (The Al matrix is an fcc structure with lattice constant a = 0.406 nm) is coherent with matrix. θ'-Al$_2$Cu (fcc lattice, a = 0.404 nm, c = 0.580 nm) [12] with a misfit of 0.5%, is semi-coherent with matrix. θ-Al$_2$Cu (C16 lattice, a = 0.607 nm, c = 0.487 nm) with a misfit of 20%, is incoherent with matrix [11]. Such interfaces are generated to release the misfit strain.

Figure 9e–g quantify the correlation among the evolutions of structure, strain energy, and composition. Here, we calculate the averaged misfit strain energy around nucleation sites. All the strain energy curves initially increase gently at the stage of solute segregation, then reach a maximum due to spinodal decomposition, and finally decrease after the formation of new solid phases. By combining the atomic configurations in Fig. 9a–d and the time evolution of

Figure 9 The strain distribution during GB precipitation. **a** Low-angle tilt GB with lattice misfit 19%; **b** Low-angle tilt GB with lattice misfit 15%; **c** high-angle tilt GB with lattice misfit 19%; **d** High-angle tilt GB with lattice misfit 15%. **e** The time evolution of strain (ε_1 and ε_2) and concentration evolution (c_1 and c_2) on low angle GB. **f** The time evolution of strain (ε_1 and ε_2) and concentration (c_1 and c_2) on high angle GB. **g** The critical concentration of structure transformation and the lattice misfit. The curves ε_1 and ε_2 indicate the strain evolution on relatively low lattice misfit (15%) and relatively high lattice misfit (19%) samples, respectively. The curves c_1 and c_2 indicate the concentration evolution on relatively low lattice misfit (15%) and relatively high lattice misfit (19%) samples, respectively.
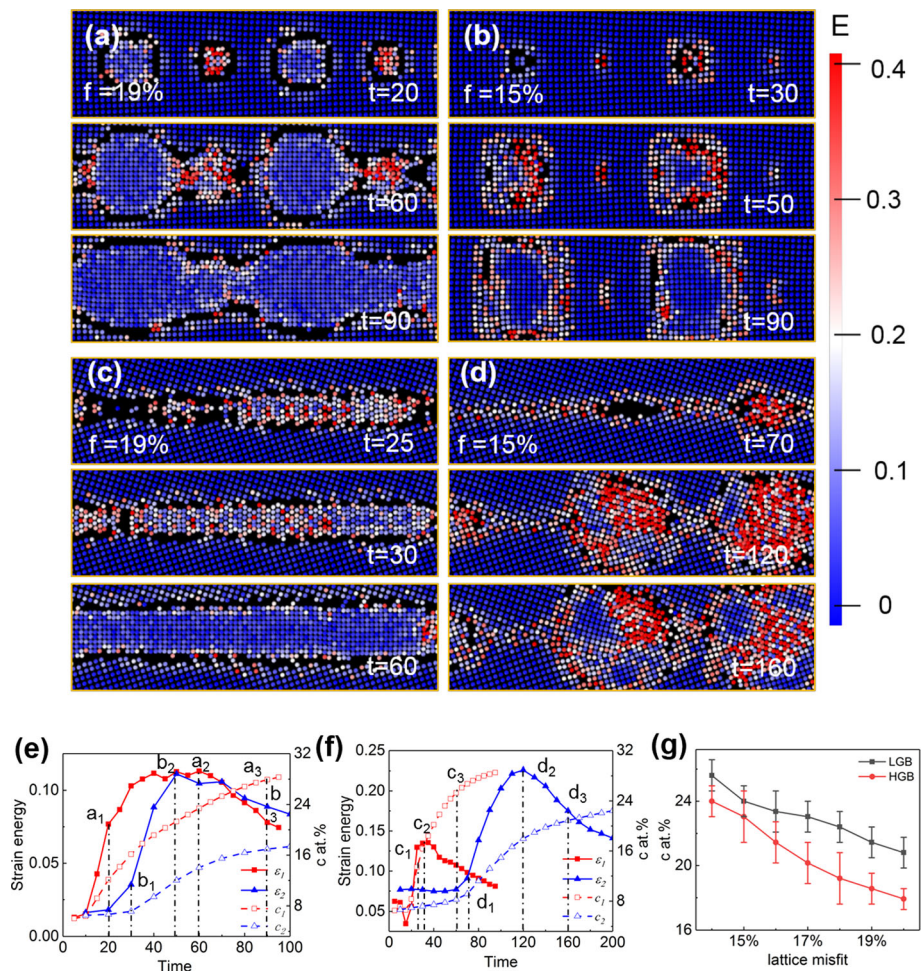
misfit strain energy in Fig. 9e and f, we find that the accumulation of solute concentration at the early stage of nucleation increases the local strain substantially, and then, on the contrary, the structure evolution involving the formation of new phases (e.g., amorphous phase and precipitates) can release some misfit strain. A higher lattice misfit results in a higher enrichment rate of concentration at the early stage of clustering, as we mentioned above in Fig. 7; thus, a higher increase rate of misfit strain simultaneously, as shown in Fig. 9e and f, and finally shorter incubation time for new solid phases. The formation of a new solid phase can relax the misfit strain. Therefore, the increased rate of misfit strain of the samples with higher lattice misfits slows down much earlier.

Finally, we investigate in Fig. 9g the dependence of the critical concentration at the onset of cluster nucleation on lattice misfit. The critical concentration required by the triggering of structure transformation tends to decrease as the lattice misfit increases. A higher lattice misfit means that a smaller amount of solute can bring sufficient strain energy to trigger structure transformation, contributing to a smaller nucleation barrier. This is consistent with the results that the work of formation decreases with lattice misfit, as shown in Fig. 3b. These results explain why the increase in lattice misfit is more conducive to the nucleation of precipitates and favors the layer growth mode.

Conclusion

In this work, we systematically investigate the effects of lattice misfits on GB precipitation by using the PFC model. GB precipitation processes tuned by the magnitude of lattice misfit and GB structures are successfully simulated on the atomic scale in the context of aluminum alloys. Our main conclusions are as follows.

We find that lattice misfit correlate closely with the growth modes of GB precipitates. The island growth mode tends to be prevalent with decreasing lattice misfits or GB misorientation, while the layer growth tends to be prevalent with increasing lattice misfits or GB misorientation. At a relatively low lattice misfit, GB segregation and spinodal decomposition first lead to the periodic distribution of solute, then nucleation events at solute-enriched sites, and island growth

mode consequently. In contrast, at a sufficiently high lattice misfit, the increase in lattice misfits makes nucleation occur at a lower concentration, which gives rise to the rapid merging of densely distributed nuclei, and then layer growth occurs. It is quantified that a higher lattice misfit makes a smaller amount of solute able to bring sufficient strain energy to trigger structure transformation, contributing to a smaller nucleation barrier.

Taken as a whole, our work reveals that lattice misfit can profoundly affect the nucleation kinetics, growth mode, and morphology of precipitates, and, more subtly, the interactions among structural, compositional, and misfit strain evolutions. This work theoretically suggests that the precipitation behavior and precipitation microstructure vary substantially with the lattice misfit between the precipitates and the matrix phase. As a result, the formation and microstructure of precipitates in aluminum alloys are often very different. Moreover, a comprehensive understanding of the dependences of precipitation on lattice misfit can potentially provide clues in the composition design and microstructure control for precipitation-strengthening aluminum alloys.

Acknowledgements

Date availability

The simulation data from this study are available from the corresponding author upon reasonable request.

Code availability

All code used to calculate the current results is available from the corresponding author upon reasonable request.

Declarations

Conflict of interest The authors declare no competing financial or nonfinancial interests.

References

[1] Small KA, Clayburn Z, DeMott R, Primig S, Fullwood D, Taheri, ML (2020) Interplay of dislocation substructure and elastic strain evolution in additively manufactured Inconel 625 - Sciencedirect. Mater Sci Eng: A 785:139380

[2] Xiao L, Chen X, Wei K, Liu Y, Yin D, Hu Z, Zhou H, Zhu Y (2021) Effect of dislocation configuration on Ag segregation in subgrain boundary of a Mg-Ag alloy. Scripta Mater 191:219–224

[3] Lee SW, Kim JH, Park CH, Hong J-K, Yeom J-T (2021) Alloy design of metastable α+β titanium alloy with high elastic admissible strain. Mater Sci Eng: A 802:140621. https://doi.org/10.1016/j.msea.2020.140621

[4] Tonks M, Millett P, Cai W, Wolf D (2010) Analysis of the elastic strain energy driving force for grain boundary migration using phase field simulation. Scripta Mater 63(11):1049–1052. https://doi.org/10.1016/j.scriptamat.2010.07.034

[5] Alves CLM, Rezende J, Senk D, Kundin J (2020) Phase-field simulation of peritectic steels solidification with transformation-induced elastic effect. J Market Res 9(3):3805–3816. https://doi.org/10.1016/j.jmrt.2020.02.007

[6] El-Ghazzawy EH (2020) Effect of heat treatment on structural, magnetic, elastic and optical properties of the co-precipitated Co0.4Sr0.6Fe2O4. J Magn Magn Mater 497:166017. https://doi.org/10.1016/j.jmmm.2019.166017

[7] Javanbakht M, Adaei M (2019) Investigating the effect of elastic anisotropy on martensitic phase transformations at the nanoscale. Comput Mater Sci 167:168–182. https://doi.org/10.1016/j.commatsci.2019.05.047

[8] Motazedian F, Zhang J, Wu Z, Jiang D, Sarkar S, Martyniuk M, Yan C, Liu Y, Yang H (2021) Achieving ultra-large elastic strains in Nb thin films on NiTi phase-transforming substrate by the principle of lattice strain matching. Mater Des 197:109257. https://doi.org/10.1016/j.matdes.2020.109257

[9] Sun J, Hensel J, Klassen J, Nitschke-Pagel T, Dilger K (2019) Solid-state phase transformation and strain hardening on the residual stresses in S355 steel weldments. J Mater Process Technol 265:173–184. https://doi.org/10.1016/j.jmatprotec.2018.10.018

[10] Zhang F, Zhang G, Yang L, Zhou Y, Du Y (2019) Thermodynamic modeling of YO1.5-TaO2.5 system and the effects of elastic strain energy and diffusion on phase transformation of YTaO4. J Eur Ceram Soc 39(15):5036–5047. https://doi.org/10.1016/j.jeurceramsoc.2019.07.008

[11] Wang Q, Li Z, Pang S, Li X, Dong C, Liaw PK (2018) Coherent precipitation and strengthening in compositionally complex alloys: a review. Entropy (Basel) 20(11):878. https://doi.org/10.3390/e20110878

[12] Zhou CLWL, Xie P, Niu FJ, Ming WQ, Du K, Chen JH (2021) A hidden precipitation scenario of the θ′-phase in Al-Cu alloys. J Mater Sci Technol 75:126–138. https://doi.org/10.1016/j.jmst.2020.09.039

[13] Chrominski W, Lewandowska M (2020) Influence of dislocation structures on precipitation phenomena in rolled Al–Mg–Si alloy. Mater Sci Eng, A 793:139903. https://doi.org/10.1016/j.msea.2020.139903

[14] Brauer G (1939) Über die kristallstruktur von TiAl3, NbAl3, TaAl3, und ZrAl3, Z. Anorg Allg Chem 242:1–22

[15] Norby ANCP (1986) Preparation and structure of Al3Ti. Acta Chem Scand Ser A 40:157–159

[16] Srinivasan PBDS, Schwarz RB (1991) Metastable phases in the Al3X (X = Ti, Zr, and Hf) intermetallic system. Scr Metall Mater 25(11):2513–2516

[17] Lee SB, Jung J, Yoo SJ, Kim Y, Han HN (2019) Effects of coherency strain on structure and migration of a coherent grain boundary in Cu. Mater Charact 151:436–444. https://doi.org/10.1016/j.matchar.2019.02.042

[18] Gelczuk Ł, Serafińczuk J, Dąbrowska-Szata M, Dłużewski P (2008) Anisotropic misfit strain relaxation in lattice mismatched InGaAs/GaAs heterostructures grown by MOVPE. J Cryst Growth 310(12):3014–3018. https://doi.org/10.1016/j.jcrysgro.2008.03.003

[19] Ahn SY, Kim SW, Kang S (2010) Microstructure of Ti(CN)–WC–NbC–Ni Cermets. J Am Ceram Soc 84(4):843–849

[20] Kim S, Zuo J-M, Kang S (2010) Effect of WC or NbC addition on lattice parameter of surrounding structure in Ti(C0.7N0.3)–Ni cermets investigated by TEM/CBED. J Eur Ceram Soc 30(10):2131–2138. https://doi.org/10.1016/j.jeurceramsoc.2010.03.006

[21] Wen H, Zhao B, Dong X, Sun F, Zhang L (2020) Preferential growth of coherent precipitates at grain boundary. Mater Lett 261:126984. https://doi.org/10.1016/j.matlet.2019.126984

[22] Ferreirós PA, Alonso PR, Rubiolo GH (2019) Effect of Ti additions on phase transitions, lattice misfit, coarsening, and hardening mechanisms in a Fe2AlV-strengthened ferritic alloy. J Alloys Compd 806:683–697. https://doi.org/10.1016/j.jallcom.2019.07.288

[23] Neumeier S, Pyczak F, Göken M (2021) The temperature dependent lattice misfit of rhenium and ruthenium containing nickel-base superalloys – experiment and modelling. Mater

Des 198:109362. https://doi.org/10.1016/j.matdes.2020.109362

[24] Liu X, Chen Z, Chen Y, Yang S, Pan Y, Lu Y, Qu S, Li Y, Yang Y, Wang C (2021) Multicomponent Co-Ti-based superalloy with high solvus temperature and low lattice misfit. Mater Lett 284:128910. https://doi.org/10.1016/j.matlet.2020.128910

[25] He F, Zhang K, Yeli G, Tong Y, Wei D, Li J, Wang Z, Wang J, Kai JJ (2020) Anomalous effect of lattice misfit on the coarsening behavior of multicomponent L12 phase. Social Ence Electron Publ 183:111–116

[26] Ramanarayan H, Abinandanan TA (2003) Phase field study of grain boundary effects on spinodal decomposition. Acta Mater 51(16):4761–4772. https://doi.org/10.1016/s1359-6454(03)00301-x

[27] Li L, Li Z, Kwiatkowski Da Silva A, Peng Z, Zhao H, Gault B, Raabe D (2019) Segregation-driven grain boundary spinodal decomposition as a pathway for phase nucleation in a high-entropy alloy. Acta Mater 178:1–9. https://doi.org/10.1016/j.actamat.2019.07.052

[28] Ramanarayan H, Abinandanan TA (2004) Grain boundary effects on spinodal decomposition. Acta Mater 52(4):921–930. https://doi.org/10.1016/j.actamat.2003.10.028

[29] Guo C, Shi Y, Chen J, Xiao X, Liu B, Liu J, Yang B (2020) Effects of P addition on spinodal decomposition and discontinuous precipitation in Cu-15Ni-8Sn alloy. Mater Charact 171:110760. https://doi.org/10.1016/j.matchar.2020.110760

[30] Maji R, Luppi E, Capron N, Degoli E (2021) Ab initio study of oxygen segregation in silicon grain boundaries: the role of strain and vacancies. Acta Mater 204:116477. https://doi.org/10.1016/j.actamat.2020.11.019

[31] Soenen B, De AK, Vandeputte S, De Cooman BC (2004) Competition between grain boundary segregation and Cottrell atmosphere formation during static strain aging in ultra low carbon bake hardening steels. Acta Mater 52(12):3483–3492. https://doi.org/10.1016/j.actamat.2004.03.046

[32] Sun Z, Tan X, Wang C, Descoins M, Mangelinck D, Tor SB, Jägle EA, Zaefferer S, Raabe D (2020) Reducing hot tearing by grain boundary segregation engineering in additive manufacturing: example of an AlxCoCrFeNi high-entropy alloy. Acta Mater. 204:116505. https://doi.org/10.1016/j.actamat.2020.116505

[33] Wu YX, Li XY, Wang YM (2007) First-principles study of the influence of lattice misfit on the segregation behaviors of hydrogen and boron in the Ni–Ni3Al system. Acta Mater 55(14):4845–4852. https://doi.org/10.1016/j.actamat.2007.05.006

[34] Luo L, Ma Y, Li S, Pei Y, Qin L, Gong S (2018) Evolutions of microstructure and lattice misfit in a γ'-rich Ni-based superalloy during ultra-high temperature thermal cycle. Intermetallics 99:18–26. https://doi.org/10.1016/j.intermet.2018.05.011

[35] Wang H, Gao X, Chen S, Li Y, Wu Z, Ren H (2020) Effects of Al on the precipitation of B2 Cu-rich particles in Fe–Cu ferritic alloy: experimental and theoretical study. J Alloys Compd 846:156386. https://doi.org/10.1016/j.jallcom.2020.156386

[36] Alrababah YM, Sheng CK, Hassan MF (2019) Influence of ammonium nitrate concentration on structural evolution and optical properties tuning of CdS nanoparticles synthesized by precipitation method. Nano-Struct Nano-Obj 19:100344. https://doi.org/10.1016/j.nanoso.2019.100344

[37] Mao H, Kong Y, Cai D, Yang M, Peng Y, Zeng Y, Zhang G, Shuai X, Huang Q, Li K, Zapolsky H, Du Y (2020) β" needle-shape precipitate formation in Al-Mg-Si alloy: phase field simulation and experimental verification. Comput Mater Sci 184:109878. https://doi.org/10.1016/j.commatsci.2020.109878

[38] Riet AA, Van Orman JA, Lacks DJ (2021) A molecular dynamics study of grain boundary diffusion in MgO. Geochim Cosmochim Acta 292:203–216. https://doi.org/10.1016/j.gca.2020.09.012

[39] Deymier P, Taiwo A, Kalonji G (1987) A grain boundary phase transition studied by molecular dynamics. Acta Metall 35(11):2719–2730. https://doi.org/10.1016/0001-6160(87)90271-9

[40] Guziewski M, Banadaki AD, Patala S, Coleman SP (2020) Application of Monte Carlo techniques to grain boundary structure optimization in silicon and silicon-carbide. Comput Mater Sci 182:109771. https://doi.org/10.1016/j.commatsci.2020.109771

[41] Mohammadi H, Eivani AR, Seyedein SH, Ghosh M (2020) Modified Monte Carlo approach for simulation of grain growth and Ostwald ripening in two-phase Zn–22Al alloy. J Market Res 9(5):9620–9631. https://doi.org/10.1016/j.jmrt.2020.06.017

[42] Elder KR, Katakowski M, Haataja M, Grant M (2002) Modeling elasticity in crystal growth. Phys Rev Lett. https://doi.org/10.1103/physrevlett.88.245701

[43] Elder KR, Grant M (2004) Modeling elastic and plastic deformations in nonequilibrium processing using phase field crystals. Phys Rev E. https://doi.org/10.1103/physreve.70.051605

[44] Elder KR, Provatas N, Berry J, Stefanovic P, Grant M (2007) Phase-field crystal modeling and classical density functional theory of freezing. Phys Rev B. https://doi.org/10.1103/physrevb.75.064107

[45] Greenwood M, Rottler J, Provatas N (2011) Phase-field-crystal methodology for modeling of structural transformations. Phys Rev E. https://doi.org/10.1103/physreve.83.031601

[46] Tang S, Wang JC, Svendsen B, Raabe D (2017) Competitive bcc and fcc crystal nucleation from non-equilibrium liquids studied by phase-field crystal simulation. Acta Mater 139:196–204. https://doi.org/10.1016/j.actamat.2017.08.015

[47] Gránásy L, Tóth GI, Warren JA, Podmaniczky F, Tegze G, Rátkai L, Pusztai T (2019) Phase-field modeling of crystal nucleation in undercooled liquids – a review. Prog. Mater Sci. 106:100569. https://doi.org/10.1016/j.pmatsci.2019.05.002

[48] Backofen R, Barmak K, Elder KE, Voigt A (2014) Capturing the complex physics behind universal grain size distributions in thin metallic films. Acta Mater 64:72–77. https://doi.org/10.1016/j.actamat.2013.11.034

[49] Wu K-A, Voorhees PW (2012) Phase field crystal simulations of nanocrystalline grain growth in two dimensions. Acta Mater 60(1):407–419. https://doi.org/10.1016/j.actamat.2011.09.035

[50] Tang S, Wang Z, Guo Y, Wang J, Yu Y, Zhou Y (2012) Orientation selection process during the early stage of cubic dendrite growth: a phase-field crystal study. Acta Mater 60(15):5501–5507. https://doi.org/10.1016/j.actamat.2012.07.012

[51] Tang S, Wang J, Li J, Wang Z, Guo Y, Guo C, Zhou Y (2017) Phase-field-crystal investigation of the morphology of a steady-state dendrite tip on the atomic scale. Phys Rev E. https://doi.org/10.1103/physreve.95.062803

[52] Shuai X, Wang ZJ, Mao H, Tang S, Kong Y, Du Y (2021) Atomic-scale study of compositional and structural evolution of early-stage grain boundary precipitation in Al–Cu alloys through phase-field crystal simulation. J Mater Sci 56(22):12700–12715. https://doi.org/10.1007/s10853-021-06064-0

[53] Fallah V, Korinek A, Ofori-Opoku N, Provatas N, Esmaeili S (2013) Atomistic investigation of clustering phenomenon in the Al–Cu system: three-dimensional phase-field crystal simulation and HRTEM/HRSTEM characterization. Acta Mater 61(17):6372–6386. https://doi.org/10.1016/j.actamat.2013.07.015

[54] Fallah V, Ofori-Opoku N, Stolle J, Provatas N, Esmaeili S (2013) Simulation of early-stage clustering in ternary metal alloys using the phase-field crystal method. Acta Mater 61(10):3653–3666. https://doi.org/10.1016/j.actamat.2013.02.053

[55] Yamanaka A, McReynolds K, Voorhees PW (2017) Phase field crystal simulation of grain boundary motion, grain rotation and dislocation reactions in a BCC bicrystal. Acta Mater 133:160–171. https://doi.org/10.1016/j.actamat.2017.05.022

[56] Joel Berry NP, Rottler J, Sinclair CW (2012) Defect stability in phase-field crystal models: stacking faults and partial dislocations. Phys Rev B 86:241142. https://doi.org/10.1103/PhysRevB.86.224112

[57] Joel Berry NP, Rottler J, Sinclair CW (2014) Phase field crystal modeling as a unified atomistic approach to defect dynamics. Phys Rev B 89:214117. https://doi.org/10.1103/PhysRevB.89.214117

[58] Greenwood M, Rottler J, Provatas N (2011) Phase-field-crystal methodology for modeling of structural transformations. Phys Rev E Stat Nonlinear Soft Matter Phys 83(1):031601

[59] Chen LQ, Jie S (1998) Applications of semi-implicit Fourier-spectral method to phase field equations. Comput Phys Commun 108(2–3):147–158

[60] Saha S, Todorova TZ, Zwanziger JW (2015) Temperature dependent lattice misfit and coherency of Al3X (X = Sc, Zr, Ti and Nb) particles in an Al matrix. Acta Mater 89:109–115. https://doi.org/10.1016/j.actamat.2015.02.004

[61] Liu C, Garner A, Zhao H, Prangnell PB, Gault B, Raabe D, Shanthraj P (2021) CALPHAD-informed phase-field modeling of grain boundary microchemistry and precipitation in Al-Zn-Mg-Cu alloys. Acta Mater 214:116966. https://doi.org/10.1016/j.actamat.2021.116966

[62] Raabe SSBD, Millan J, Ponge D, Assadi H, Herbig M, Choi P-P (2013) Segregation engineering enables nanoscale martensite to austenite phase transformation at grain boundaries: A pathway to ductile martensite. Acta Mater 61:6132–6152. https://doi.org/10.1016/j.actamat.2013.06.055

[63] Sun S, Zhao E, Hu C, An Y, Chen W (2021) Precipitation behavior of silicide and synergetic strengthening mechanisms in TiB-reinforced high-temperature titanium matrix composites during multi-directional forging. J Alloys Compd 867:159051. https://doi.org/10.1016/j.jallcom.2021.159051

[64] Xiao-juan Wang L, Huang T-W, Yang W-C, Yue Q-Z, He C, Zhang J, ZhiFu H (2020) Grain boundary precipitation behavior in Re-containing nickel-based directionally solidified superalloys with carbon and boron additions. Vacuum 179:109483. https://doi.org/10.1016/j.vacuum.2020.109483

[65] Kuzmina M, Herbig M, Ponge D, Sandlobes S, Raabe D (2015) Linear complexions: confined chemical and structural states at dislocations. Science 349(6252):1080–1083. https://doi.org/10.1126/science.aab2633

[66] Guo Y, Wang J, Wang Z, Li J, Tang S, Liu F, Zhou Y (2015) Strain mapping in nanocrystalline grains simulated by phase

field crystal model. Philos Mag 95(9):973–984. https://doi.org/10.1080/14786435.2015.1011250

[67] Galindo PL, Kret S, Sanchez AM, Laval J-Y, Yáñez A, Pizarro J, Guerrero E, Ben T, Molina SI (2007) The peak pairs algorithm for strain mapping from HRTEM images. Ultramicroscopy 107(12):1186–1193. https://doi.org/10.1016/j.ultramic.2007.01.019

Publisher's Note Springer Nature remains neutral with regard to jurisdictional claims in published maps and institutional affiliations.